

# DWA-3D: A Reactive Planner for Robust and Efficient Autonomous UAV Navigation

Jorge Bes, Juan Dendarieta, Luis Riazuelo, Luis Montano.

*Instituto de Investigación en Ingeniería de Aragón (I3A), University of Zaragoza, Spain  
montano@unizar.es*

## Abstract

Despite the growing impact of Unmanned Aerial Vehicles (UAVs) across various industries, most of current available solutions lack for a robust autonomous navigation system to deal with the appearance of obstacles safely. This work presents an approach to perform autonomous UAV planning and navigation in scenarios in which a safe and high maneuverability is required, due to the cluttered environment and the narrow rooms to move. The system combines an RRT\* global planner with a newly proposed reactive planner, *DWA-3D*, which is the extension of the well known *DWA* method for 2D robots. We provide a theoretical-empirical method for adjusting the parameters of the objective function to optimize, easing the classical difficulty for tuning them. An onboard LiDAR provides a 3D point cloud, which is projected on an Octomap in which the planning and navigation decisions are made. There is not a prior map; the system builds and updates the map online, from the current and the past LiDAR information included in the Octomap. Extensive real-world experiments were conducted to validate the system and to obtain a fine tuning of the involved parameters. These experiments allowed us to provide a set of values that ensure safe operation across all the tested scenarios. Just by weighting two parameters, it is possible to prioritize either horizontal path alignment or vertical (height) tracking, resulting in enhancing vertical or lateral avoidance, respectively. Additionally, our *DWA-3D* proposal is able to navigate successfully even in absence of a global planner or with one that does not consider the drone's size. Finally, the conducted experiments show that computation time with the proposed parameters is not only bounded but also remains stable around 40ms, regardless of the scenario complexity.

*Keywords:* UAV, Drone, 3D Reactive Navigation, 3D Planning, 3D Occupancy Map

## 1. Introduction

Unmanned Aerial Vehicles (UAVs) market is experiencing an outstanding growth [1] in the last years driven by their versatility and ability to access difficult or dangerous locations. From mine inspection [2] and infrastructure maintenance [3] to logistics [4] and agriculture [5] or even search-and-rescue missions [6], UAVs are transforming industries. While most applications thrive in open environments with neglectable collision risk, venturing into more complex areas demands robust autonomous navigation solutions due to the severe consequences that a potential crash would involve. Those needs became evident when the US Defence Advanced Research Projects Agency (DARPA) funded with \$82 million the *DARPA Subterranean Challenge*, which focused on navigation in hazardous scenarios like caves.

Previous approaches to fully integrate an autonomous UAV navigation system have already been presented,

like the one in [7], where the local planner changes the plan computed by the global when an obstacle interrupts the line of sight between waypoints. Although their results seem promising, no dynamic constraints are considered during the replanning and their real experiments lack of complexity. A NMPC perception-based reactive navigation method with real experimentation is proposed in [8] and integrated with a 3D Artificial Potential Field in [9], enabling also human-safe interactions. Although the 3D environment is taken into account, they do not exploit the vertical motion capabilities of the UAV during obstacle evasion, which may be mandatory in unstructured and uneven environments as caves. Two vision-based approaches with fast maneuver capabilities are presented in [10] and [11], but due to depth cameras range limitations its application is neglected in critical low-visibility scenarios, hindering safe operation. In the latter, a JPS (Jump Point Search)

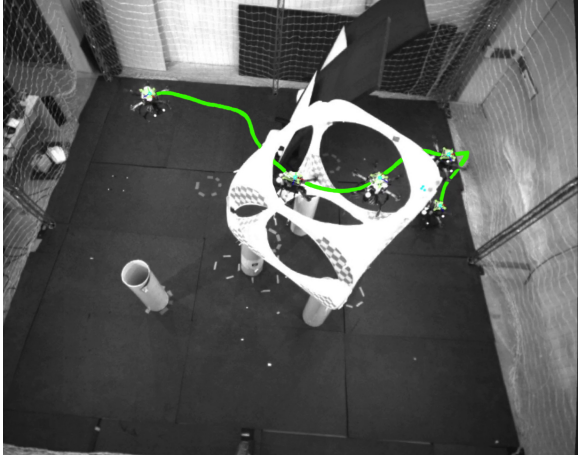


Figure 1: Our hexarotor performing an autonomous flight maneuvering in the *Rings Scenario*.

is used as a global planner, and third-degree polynomial trajectories are computed by optimizing a constrained function and a triple integrator model for moving the drone at high speed. The optimization algorithm iterates until convergence, therefore the computational time is not a priori bounded, and new subgoal recomputation is needed in these cases. Moreover, the method needs the global plan for re-computing feasible trajectories. An obstacle avoidance method based on RMS (Riemannian Motion Policies), feasible for both volumetric maps and raw 3D LiDAR scans is shown in [12], where high control rates are attained thanks to GPU raycasting operations and concurrency. It exploits the massive parallel policies combination and raycasting in a voxel-based map. As a local planner, the method also falls sometimes in local minima, because it there is not integrated with a global planner. However, complex scenarios are only tested in simulation, and only a simpler scenario for a real experiment is achieved. The work in [13] combines a collision detector with a RRT\* global planner for drone navigation but both, the method and the simulations are developed for a 2D horizontal navigation. [14] integrates a RRT-Connect global planner with a collision detector that uses the distance to the obstacle and a sliding mode based reactive controller to avoid the closest obstacle, returning to the path planned when the obstacle is far from that distance. [15] addresses a LiDAR-based drone navigation for underground tunnels, using a bio-inspired nearness detection and a reactive proportional control for the velocities and the *Yaw* angle. The work does not consider a true avoidance of obstacles in the way, only the walls of the tunnel. [16] combines an optimal control solved as a nonlin-

ear problem for obstacle avoidance with a MPC and a low-level PID controller for navigating in environments with many obstacles. The paper neither provides the computation time to evaluate the real-time performance to be applied in real experiments, nor drone trajectories among the obstacles. These methods have been evaluated in simulation and considering the map and the obstacle location are completely known beforehand.

The Dynamic Window Approach (DWA) [17] is a well known solution to the 2D reactive navigation problem that has been widely used since it was proposed in 1997. Despite being a reliable and reference method, it still has not been proposed to extend it to the 3D search space for UAVs, as far as the authors are concerned. Two proposals for submarine vehicles are presented in [18] and [19] where only simulated experiments are performed. In [20] the original 2D DWA is combined with 3DVFH+ to perform multi-UAV obstacle avoidance. Nevertheless, their DWA is limited to the 2D plane, computing the velocity in Z axis out of the 2D velocity optimization achieved by DWA. The work lacks of real experimentation, being the simulation scenarios with obstacles very simple. Moreover, the authors do not provide hints about how to tune the values of the multiple parameters the method includes.

Our work focuses on the development of a new local planner, DWA-3D, for scenarios in which a drone has to maneuver among nearby obstacles distributed in the environment. The local planner is integrated with a state of the art global planner, RRT\* [21]. Planning and navigation make decisions on an occupancy map (Octomap [22]) built from the environment real time information provided by an onboard 3D LiDAR. Real-world experiments have been performed with a custom hexarotor (see Figure 1) equipped with a LiDAR Ouster OS032. The experimentation and evaluation has been made in an indoor Arena scenario in order to achieve a fine tuning of the method. The final aim is to experiment in larger indoor buildings, caves, underground mazes or dense urban areas, which will be made in a future work.

The main contributions are:

- We have developed a novel technique, DWA-3D, solved as an optimization in a velocity space. The dynamic constraints, in terms of capability of acceleration-deceleration, are implicit in the method, therefore only feasible commands are computed every control period. The drone can maneuver in scenarios with lateral, top or bottom obstacles, making the best (optimal for the objective function) avoidance maneuver depending on two decision parameters.

- Unlike in the classical 2D method, a non uniform distance computation to obstacles has been proposed, to enhance them as a function of the relative position and orientation with respect to the drone forward motion. The dense point could LiDAR information is condensed in a voxel-map representation, which allows to reduce strongly the computation time in the optimization, without loosing relevant obstacle information. Moreover, this approach allows the reactive planner to consider the past observed information to make decisions, instead of directly using the point cloud in the current sampling period for a pure reactive behaviour.
- An ample set of exhaustive real-world experiments in different kind of scenarios have been performed, which allowed to qualitatively evaluate the method. From this evaluation, we provide a set of default parameters, whose constraints have been analytically established.

The computational time is around 40ms despite the scenario complexity, allowing to perform real-time control of the UAV and react to unexpected obstacles in the path. During real-world experiments, the proposed DWA-3D reactive planner was integrated alongside three global planner variants to address the challenges posed by frequent recomputations in partially observed or dynamic environments. These variants included a naive planner, a drone-size-agnostic planner, and a safer drone-size-aware planner. The capability of DWA-3D local planner of making the last and safer decisions about the best velocity command to apply, has been evaluated in the three cases, concluding its robustness in all the scenarios evaluated. DWA-3D computes commands to follow or not the global planned path, according with the new information incoming from the sensors every control period and the feasibility and safety of the resulting motion estimated in the optimization. The architecture has been implemented in ROS [23]. The authors commit to release a well-tested and configurable code both for simulation and real experimentation once the publication is accepted.

## 2. System overview

Our proposal supposes that the perception provides 3D pointclouds (from a 3D LiDAR or a depth camera) and that a map can be built from them, allowing to query about occupancy or distances to obstacles in a fast and efficient way (Octomap [22] has been our choice).

To obtain a precise drone localization, a motion capture system (Optitrack) is used. This allows to decouple the localization problem from the navigation one, being the latter the objective of the work.

Thinking in many of the drone missions in which a continuous frontal observation of the environment is desired, the method will enforce forward motion and avoid pure lateral movements. Therefore, only motions in the robocentric reference X, and Z axes, and the rotation around Z axis (Yaw) are allowed as control actions.

Figure 2 shows a schematic representation of the integrated navigation system and the components involved.

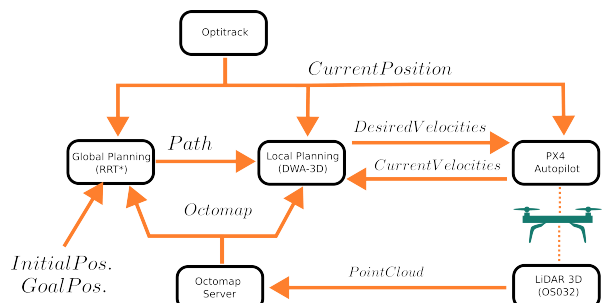


Figure 2: System General Scheme.

First, the path planning (also known as global planning) computes a set of waypoints that guide the robot to the goal location. This component is the one that is executed at the lowest rate, as it is the most expensive and once it has been computed remains valid for a longer period of time than the others.

Then, the local planner is in charge of aligning the path computed by the global planner, ensuring not only that the desired route is followed as precisely as possible, but also that the dangers and the sudden changes along it are avoided in a reactive way. Moreover, one of the objectives of the work is to evaluate the capability of the local planner to manage and make decisions about the best motion every sampling time, even in the case of using a very simple global planner, or because a low frequency re-planning is achieved, or reacting in changing environments in which the global path could temporally invade the area occupied by the moving obstacles. This part of the system must work in real time and will compute the actions needed to perform the trajectory.

The low-level onboard control obeys the linear and angular velocity commands sent by the reactive navigator, moving the drone and allowing the sensors to perceive a new fragment of the world and update the map.

Some of our main requirements are system modularity, flexibility and accessibility; avoiding strong dependencies between the building blocks while enhancing the substitution of any of them if needed. Thus, the code has been implemented in ROS, using common messages types to communicate the different subparts involved.

### 3. Map Representation

The environment around the robot must be stored in order to use it both in global and local planning. As 3D LiDAR pointclouds tend to be too dense, it is advisable to compress the information before giving it to both planners. The selected representation system has been Octomap [22], a 3D occupancy grid map that can be built online ( $7\text{Hz}$ ). Moreover, it updates already known areas if there is any change, allowing to make reactive navigation even with moving obstacles. Figure 3 shows an example of the transition from the real world environment to the captured pointcloud and the resulting Octomap representation. A voxel size of  $10\text{cm}$  has been chosen, balancing computation load and information loss; reducing the map density from 32768 points per each LiDAR scan to just 1000 voxels per  $\text{m}^3$ . Furthermore, this data structure allows for efficient occupancy queries along the space.

### 4. DWA-3D (Reactive Planner)

One of our main proposals is recovering the idea of the Dynamic Window and adapting it to an UAV for 3D navigation, by controlling advance and ascent speeds along with the rotation velocity in the horizontal plane. Additionally, the avoiding behavior can be configured, being able to select between vertical or horizontal preference. This section details the main features of the Dynamic Window Approach extended to 3D space: the search space with the velocities available and the evaluation function used to select the optimal combination of velocities.

#### 4.1. Problem formulation

Given an UAV that must follow a trajectory  $\mathcal{P}$  composed by a set of  $n$  waypoints, let  $\mathbf{x}$  be its position in the 3D space and  $\mathbf{x}_{g_i}$  the position of the current subgoal that is being tracked, both represented in the world reference  $W$ .

$$\mathcal{P} = \{\mathbf{g}_1, \dots, \mathbf{g}_n\} \quad (1)$$

$$\mathbf{x} = [x, y, z, \phi, \theta, \psi] \quad (2)$$

$$\mathbf{x}_{g_i} = [x_{g_i}, y_{g_i}, z_{g_i}, \phi_{g_i}, \theta_{g_i}, \psi_{g_i}] \quad (3)$$

where  $\phi_{g_i}, \theta_{g_i}, \psi_{g_i}$  are the Roll, Pitch, Yaw angles. The velocity vector of the drone in the dronecentric 3D space,  $\dot{\mathbf{x}}$ , can be expressed as

$$\dot{\mathbf{x}} = [v_x, v_y, v_z, \omega_x, \omega_y, \omega_z] \quad (4)$$

Although in our setup a 3D LiDAR is available, this is not the case for most of the aerial robots, which usually count with RGB or RGBD cameras pointing forward with a limited field of view. Thus, the navigation system takes only into account  $v_x, v_z$  and  $\omega_z$  to perform the control, neglecting  $v_y, \omega_x$  and  $\omega_y$ . Then, the control vector  $\mathbf{v}$  in the dronecentric reference can be defined as

$$\mathbf{v} = [v_x, v_z, \omega_z] \quad (5)$$

An action  $\mathbf{v}$  is selected at each iteration, being  $T$  the control period. Note that in the following subsections, the tracked waypoint will be expressed as  $\mathbf{g}$  instead of  $\mathbf{g}_i$  for the sake of readability.

#### 4.2. Search space

The  $v_x, v_z$  and  $\omega_z$  combinations must be selected between a discrete set of candidates, known as *Velocities Search Space*, Figure 4. This search space is limited and includes only the velocities that fulfill the drone's dynamics and kinematics constraints while ensuring its physical integrity, given the current robot status and the surroundings information.

##### 4.2.1. Maximum velocities space $V_s$

First of all, the search space should be restricted by the UAV's minimum and maximum velocities. These limits can be imposed by hardware capabilities or safety considerations. Additionally,  $v_x^{min} = 0$  is established to avoid backward movements, considering the typical forward-facing orientation of drone sensors. This search space,  $V_s$ , is known as *maximum velocities space*.

$$\begin{aligned} V_s = \{\mathbf{v} | & v_x \in [0, v_x^{max}] \\ & \wedge v_z \in [-v_z^{max}, v_z^{max}] \\ & \wedge \omega_z \in [-\omega_z^{max}, \omega_z^{max}]\} \end{aligned} \quad (6)$$

##### 4.2.2. Dynamic Window $V_d$

Then, the search space is further refined by considering the UAV's current velocity  $\mathbf{v}_c = [v_{c_x}, v_{c_z}, \omega_{c_z}]$  and its maximum linear and angular accelerations ( $\dot{v}_x^{max}, \dot{v}_z^{max}$  and  $\dot{\omega}^{max}$ ). This way, only reachable velocities from the actual situation after a time-step  $\Delta t$  are taken into account during the objective function optimization process. These velocities compose the *Dynamic window*

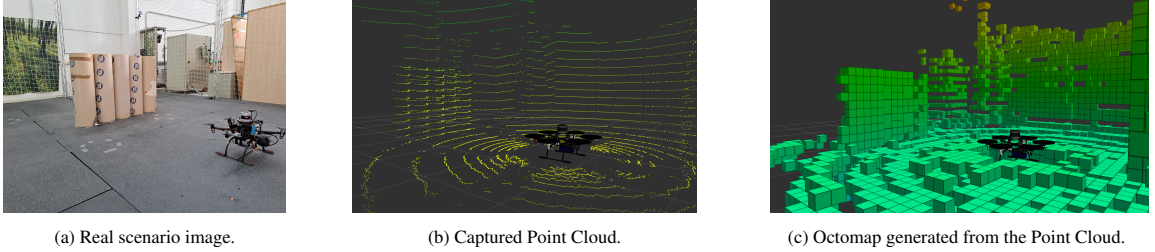


Figure 3: Steps from the real world to the Octomap environment representation.

$V_d$ , which is crucial for optimizing the objective function as it represents realistic options during the next control cycles.

$$V_d = \{\mathbf{v} | v_x \in [v_{c_x} - \dot{v}_x^{max} \cdot \Delta t, v_{c_x} + \dot{v}_x^{max} \cdot \Delta t] \\ \wedge v_z \in [v_{c_z} - \dot{v}_z^{max} \cdot \Delta t, v_{c_z} + \dot{v}_z^{max} \cdot \Delta t] \\ \wedge \omega_z \in [\omega_{c_z} - \dot{\omega}_z^{max} \cdot \Delta t, \omega_{c_z} + \dot{\omega}_z^{max} \cdot \Delta t]\} \quad (7)$$

#### 4.2.3. Admissible velocities space $V_a$

Finally, the remaining candidate velocities are evaluated to determine their collision risk. This evaluation involves predicting the drone's future positions for each candidate velocity  $\mathbf{v}$  applied during the time step  $\Delta t$ . Any of those virtual locations where the distance to the closest obstacle falls below the drone's braking distance is discarded due to collision risk. The remaining collision-free velocities form the *admissible velocities space*  $V_a$ ,

$$V_a = \{(v_x, v_z) | v_{xz} \leq \sqrt{2 \cdot d_{col} \cdot a_{max}}\} \quad (8)$$

where  $v_{xz} = \sqrt{v_x^2 + v_z^2}$ ,  $d_{col}$  is the euclidean distance from the predicted drone position to its closest obstacle and  $a_{max}$  is the maximum deceleration. The straight distance  $d_{col}$  instead of the curved one is used as a good approach, since the time-step is very short. Furthermore, it will always be smaller, thus it lowers the speed upper bound, which results in a safer navigation.

The final search space where the optimal velocity is searched in the intersection between the three spaces:  $V_r = V_s \cap V_a \cap V_d$  (Figure 4).

#### 4.3. Objective function $G(\mathbf{v})$

Once the discretized velocity search space  $V_r$  has been determined, the algorithm seeks the optimal velocity combination  $\mathbf{v}^*$  within it. This optimal velocity is chosen by maximizing the following objective function:

$$G(\mathbf{v}) = \alpha \cdot \text{Heading}(\mathbf{v}) + \beta \cdot \text{Dist}(\mathbf{v}) + \gamma \cdot \text{Vel}(\mathbf{v}) \quad (9a)$$

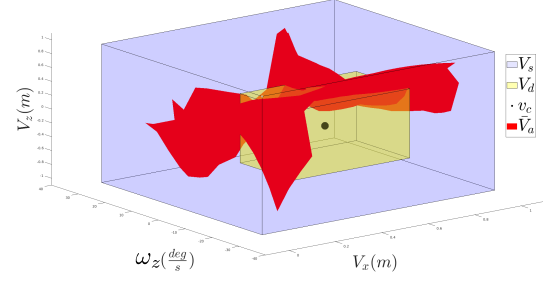


Figure 4: *Search Velocities Space*  $V_r = V_s \cap V_a \cap V_d$ . The blue area are the *Maximum velocities* ( $V_s$ ), the yellow region are the reachable velocities (*Dynamic Window*,  $V_d$ ) given the current ones (black dot,  $v_c$ ) and in red the non-admissible ones ( $\bar{V}_a$ ).

$$\mathbf{v}^* = \underset{\mathbf{v} \in V_r}{\operatorname{argmax}} G(\mathbf{v}) \quad (9b)$$

where *Heading* favours the motion towards the goal, *Dist* tries to maximize the distance to obstacles, and *Vel* the high velocities. The *Heading* term can be expanded into two terms,  $\text{Head}_z$  and  $\text{Head}_\psi$ , splitting the progress towards the goal in alignment in height and in orientation in the horizontal plane. Then, Equation 9a becomes

$$G(\mathbf{v}) = \alpha \cdot (K_\psi \cdot \text{Head}_\psi(\mathbf{v}) + K_z \cdot \text{Head}_z(\mathbf{v})) \\ + \beta \cdot \text{Dist}(\mathbf{v}) + \gamma \cdot \text{Vel}(\mathbf{v}) \quad (10)$$

This way, it is possible to tune whether staying aligned in the horizontal plane with the objective or at the same height is prioritized. As a direct consequence, if an obstacle appears between a waypoint and the UAV, it will tend to avoid it laterally if  $K_z > K_\psi$  because  $\text{Head}_z$  value will be weighted stronger. On the other hand, if  $K_\psi > K_z$ , vertical avoidance will tend to be chosen, as it will mean keeping a greater value of  $\text{Head}_\psi$ . Each term and the weights in Equation 10 are normalized between 0 and 1, and therefore the function  $G(\mathbf{v})$ ; enabling intuitive configuration of the reactive planner. Thus, the following constraints must be fulfilled,

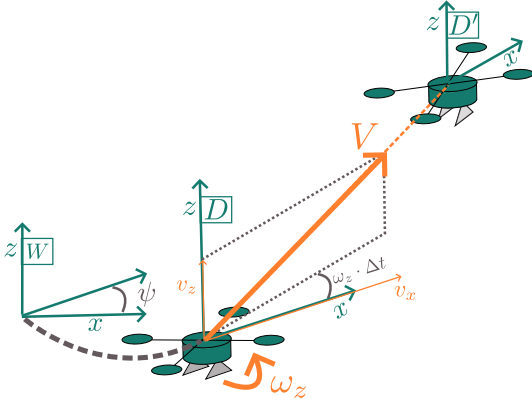


Figure 5: Predicted state of the drone after applying the selected velocities ( $v_x, v_z, \omega_z$ ).

$$\begin{cases} \alpha + \beta + \gamma = 1 \\ K_\psi + K_z = 1 \end{cases} \quad (11)$$

These functions work with the predicted position of the drone  $\mathbf{x}' = (x', y', z')$  after applying  $\mathbf{v}$  during a selected time-step  $\Delta t$  (Figure 5). As this prediction must be computed for each set of velocities in  $V_r$ , it is mandatory to speed it up the computation as much as possible while preserving its accuracy, so neither accelerations nor the effect of roll and pitch angles are taken into account. Also, the linear and angular motions are approximated as uniform ones every sampling time  $\Delta t$ ,

$$\begin{cases} \psi' = \psi + \omega_z \cdot \Delta t \\ x' = x + v_x \cdot \Delta t \cdot \cos \psi' \\ y' = y + v_x \cdot \Delta t \cdot \sin \psi' \\ z' = z + v_z \cdot \Delta t \end{cases} \quad (12)$$

being  $x, y, z$  and  $\psi$  the current values of the position and orientation of the drone pose and  $x', y', z'$  and  $\psi'$  their predicted values respectively.

The objective function  $G(\mathbf{v})$  is discretized for computing its maximum value and its corresponding optimal linear and angular velocities  $\mathbf{v}^*$  (see Equation 9b). Different discretization steps are used for the three controlled velocities in order to keep a balance between the computation time and the velocity jumps. Against other state of the art local planners that achieve non linear optimizations, the computation time is bounded, only depending on the discretization parameters. Moreover, the method directly computes optimal linear and angular velocity commands providing feasible motions under the kinodynamic constraints, according with the objective function, without the necessity of calculating complex trajectories between subgoals.

#### 4.3.1. Heading

The *Heading* term is the responsible of guiding the drone towards the goal by encouraging the alignment between them, both in the XY plane (orientation) and in height, which is a key difference from the original 2D method. Additionally, two more weights,  $K_\psi$  and  $K_z$ , are introduced. To keep with the normalization criteria, they must also add up to 1, allowing to prioritize one or the other. By tuning these weights, the preference in the avoiding behavior can be chosen. A greater value of  $K_\psi$  will prioritize staying oriented with the current subgoal, thus vertical avoidance will be preferred. In contrast, a higher value of  $K_z$  will try to keep the UAV at the same height than the current waypoint, giving more importance to lateral obstacle avoidance.

- $Head_\psi$ : It rewards velocities that help staying oriented towards the goal (Figure 6a). First the angle between the drone and the goal locations,  $\psi^{rel}$ , is computed,

$$\psi^{rel} = \text{atan2}(\Delta y, \Delta x) \quad (13a)$$

$$\Delta x = x_g - x', \quad \Delta y = y_g - y' \quad (13b)$$

being  $x_g, y_g$  the goal coordinates in the world reference. Finally, the orientation of the drone is considered to compute the normalized term (Figure 6a).

$$Head_\psi = 1 - \frac{|\psi^{rel} - \psi'|}{\pi}; \quad \psi^{rel} - \psi' \in [-\pi, \pi] \quad (14)$$

- $Head_z$ : In this case, the difference in height with respect to the tracked waypoint wants to be minimized,

$$\Delta z_i = |z_g - z'_i| \quad (15)$$

The normalization of this term is performed by finding its maximum value of those computed at the current iteration and dividing by it,

$$Head_z = 1 - \frac{\Delta z_i}{\max_i \Delta z_i} \quad (16)$$

#### 4.3.2. Distance

This term considers the obstacles that could cause a collision, penalizing those sets of velocities that are more dangerous. It is evaluated in the predicted positions by casting rays against the map up to certain distances  $L_{ij}$  (Equation 17) according to the direction of

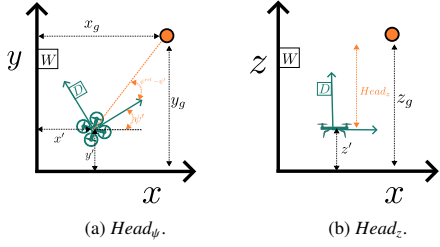


Figure 6: Graphic  $Head_\psi$  and  $Head_z$  computation for a predicted pose  $\{x', y', z'\}$ . The orange point represents the tracked waypoint.

the ray with respect to the robocentric  $X$  axis in  $D$  reference, let  $r_{\text{search}}$  be the length of the ray casted in that direction (robocentric  $X$  axis):

$$L_{ij} = r_{\text{search}} \cdot \rho_\psi^i \cdot \rho_\theta^j \quad (17)$$

$$\rho_\psi^i = 1 - \lambda_\psi \cdot \frac{|\psi_i|}{\psi_{\max}^{\text{beam}}}; \quad \rho_\theta^j = 1 - \lambda_\theta \cdot \frac{|\theta_j|}{\theta_{\max}^{\text{beam}}} \quad (18)$$

where  $\psi_i$  and  $\theta_j$  are the angles that the ray forms with the  $X$  axis of the drone in the  $XY$  and the  $XZ$  planes respectively,  $\lambda_\psi$  and  $\lambda_\theta$  parameters allow to adjust the lateral and vertical safe distances, while  $\psi_{\max}^{\text{beam}}$  and  $\theta_{\max}^{\text{beam}}$  are the maximum angles in which a ray is casted. An example of this operation can be observed in Figure 7.  $L_{ij}$  increases in the motion direction, enforcing a greater change of orientation or flying height when an obstacle is encountered near this direction, being smaller when an obstacle is detected angularly farther of that motion direction. Additionally, the beam is reoriented according to the motion direction by adding the argument of  $\vec{V} = \{v_x, 0, v_z\}$  to it, see Figure 8.

Once all the rays have been cast, the one that found an obstacle (or an unknown voxel) at the closest distance is considered for the computation of the normalized *Distance* term:

$$\text{Distance}(\mathbf{v}) = \max(0, \frac{dist_{\min} - R_{\text{drone}}}{r_{\text{search}} - R_{\text{drone}}}) \quad (19)$$

where  $R_{\text{drone}}$  is the radius of the UAV and must be taken into account to avoid collisions; as the minimum distance in the prediction position could be smaller than  $R_{\text{drone}}$  the subtraction is saturated at 0. Note that it should happen with the proper parameters configuration, but the case has been considered just in case the user commits a mistake while tuning the parameters.

Casting rays against the map instead of consulting the raw pointcloud offers not only a reduction of the elements that have to be analysed but also a more efficient way of accessing them. Additionally, the map's persistence, allows incorporating previously sensed regions,

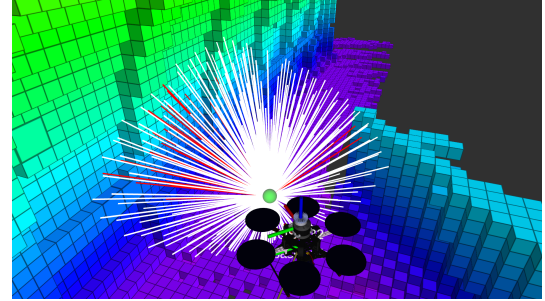


Figure 7: Example of the rays casted (white and red) from the predicted pose (green) during the distance term computation of DWA-3D. Note that the further they are from the motion direction, the shorter they are, rewarding changing the motion direction during avoidance. The red rays represent those that have found an obstacle. These shortest of the red rays is the one used for computing the Distance term in Equation 9a.

even if outside the sensor field of view, avoiding sudden dangerous reactions and oscillatory movements.

---

#### Algorithm 1 Distance term evaluation.

---

```

1: Input:  $(x', y', z', \psi', v_x, v_z, \text{Map})$ 
2: Params:  $(r_{\text{search}}, \psi_{\max}^{\text{beam}}, \theta_{\max}^{\text{beam}}, \lambda_\psi, \lambda_\theta, \delta_\psi, \delta_\theta, R_{\text{drone}})$ 
3:  $\theta_{\text{beam}} \leftarrow \text{atan2}(v_z, v_x)$ 
4:  $dist_{\min} \leftarrow r_{\text{search}}$ 
5: for  $\psi_i$  from  $-\psi_{\max}^{\text{beam}}$  to  $\psi_{\max}^{\text{beam}}$  with step  $\delta_\psi$  do
6:    $\rho_\psi \leftarrow r_{\text{search}} \cdot (1 - \lambda_\psi \cdot \frac{|\psi_i|}{\psi_{\max}^{\text{beam}}})$ 
7:   for  $\theta_j$  from  $-\theta_{\max}^{\text{beam}}$  to  $\theta_{\max}^{\text{beam}}$  with step  $\delta_\theta$  do
8:      $\rho_\theta \leftarrow r_{\text{search}} \cdot (1 - \lambda_\theta \cdot \frac{|\theta_j|}{\theta_{\max}^{\text{beam}}})$ 
9:      $L_{ij} \leftarrow r_{\text{search}} \cdot \rho_\psi \cdot \rho_\theta$ 
10:     $x_r \leftarrow \cos(\psi_i + \psi') \cdot \cos(\theta_j + \theta_{\text{beam}})$ 
11:     $y_r \leftarrow \sin(\psi_i + \psi') \cdot \cos(\theta_j + \theta_{\text{beam}})$ 
12:     $z_r \leftarrow \sin(\theta_j + \theta_{\text{beam}})$ 
13:     $ray \leftarrow (x_r, y_r, z_r)$ 
14:     $dist_{ij} \leftarrow \text{Cast ray From } (x', y', z') \text{ UpTo } L_{ij}$ 
15:     $dist_{\min} \leftarrow \min(dist_{\min}, dist_{ij})$ 
16:  end for
17: end for
18:  $Dist = \frac{dist_{\min} - R_{\text{drone}}}{r_{\text{search}} - R_{\text{drone}}}$ 
19: return  $\max(0, Dist)$ 

```

---

Finally, the term  $Dist(\mathbf{v})$  in Equation 10 is obtained from the output of Algorithm 1.

#### 4.3.3. Velocity

The velocity term makes higher speeds preferred so that the drone is forced to move, avoiding staying still when it is aligned with the goal, additionally reaching the target in the shortest possible time. Whereas high  $v_z$  values are already promoted by  $Head_z$  when there are

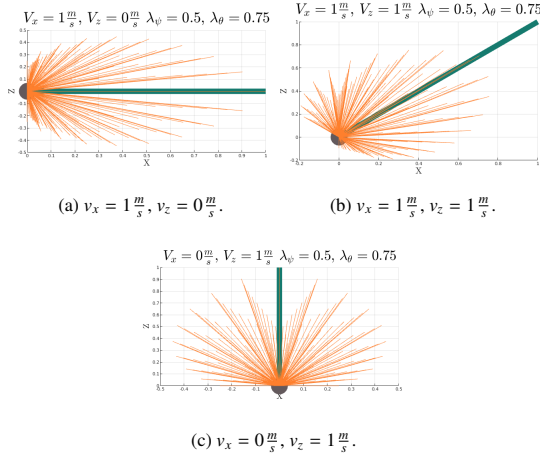


Figure 8: Ray beam (orange) reorientation according to the angle of  $\vec{V}$  (green) during the distance term computation with different  $v_x$  and  $v_z$  combinations, with  $r_{\text{search}} = 1m$ ,  $\lambda_\psi = 0.5$  and  $\lambda_\theta = 0.75$ .

significant differences between the UAV height and the waypoint one, this is not the case of  $v_x$ . According to the *Heading* preference chosen (orientation or height) the advance speed should be enhanced under certain situations:

- $K_z > K_\psi$ . Always, as it encourages the drone to move forward while maintaining its current height during lateral obstacle avoidance maneuvers.
- $K_\psi > K_z$ . Only when the waypoint is in front of the UAV, promoting forward progress while allowing to fly over and under obstacles if they are between the robot and the tracked point.

$$Vel(\mathbf{v}) = \begin{cases} \frac{v_x}{v_x^{\max}} & \text{if } K_z > K_\psi \text{ or} \\ & (Head_\psi > 0.5 \text{ and } K_z < K_\psi) \\ 0 & \text{otherwise} \end{cases} \quad (20)$$

## 5. Global Planner

The Global Planner computes a preliminary plan to follow, given the whole information known about the environment, according to certain optimization criteria that could be imposed to the system. In our case, the desired behaviour would be taking the closest path possible, thus minimizing the sum of the euclidean distance between waypoints; while being aware of not approaching too much to the obstacles taking into account the drone size (size-aware planner). That is why a safety distance can be imposed to the waypoints computed by

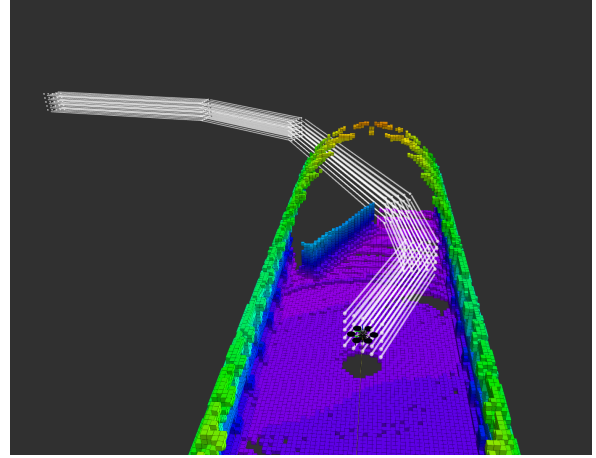


Figure 9: Example of a path (white) computed by RRT\* with the size-aware approach. On the one hand, the safety distance is checked around in the waypoints (spheres). On the other hand, a parallelepiped (lines) is casted between consecutive waypoint's safe regions.

the global planner, both by checking its surroundings and the parallelepiped that connects two consecutive waypoint's safe regions, Figure 9. Additionally, as in the local planner, it would be desirable to choose if the trajectory prefers moving laterally or vertically, so a the different global path can be computed. The following expression, is minimized during global plan computation:

$$D_{wp} = K_{length} \sum_{i=1}^{n-1} \sqrt{(x_i - x_{i+1})^2 + (y_i - y_{i+1})^2 + (z_i - z_{i+1})^2} + K_{height} \sum_{i=1}^{n-1} |z_n - z_i| \quad (21)$$

where  $n$  is the number of waypoints that conform a feasible solution with states sampled by the RRT\*,  $i$  represents the waypoints, and  $z_n$  is the Z coordinate of the goal position.  $K_{length}$  and  $K_{height}$  allow to balance between shortening the path and being at the same height than the destination. Note that although distance to obstacles is not included in Equation 5, it is considered during the optimization to discard waypoints if they involve a collision or path segments if they intersect one obstacle.

Moreover, to test the DWA-3D maneuvering capabilities under complex situations as, for instance, paths that drive the drone to move in narrow rooms, global planner's size awareness can be disabled. When deactivated, only the line of sight between waypoints is verified (not size-aware planner). In subsection 6.3, the integration

General Parameters			
Param.	Range	Rec. Value	Restrictions
$\alpha$	[0, 1]	0.3	
$\beta$	[0, 1]	0.6	
$\gamma$	[0, 1]	0.1	$\alpha + \beta + \gamma = 1$
$T$	X	100ms	
$\Delta t$	$> T$	$10 \times T = 1s$	
Avoidance Behaviour Selection			
Param.	Range	Rec. Value	Restrictions
$K_z$	[0, 1]	0.8 ( $\leftrightarrow$ avoid) 0.2 ( $\downarrow$ avoid)	
$K_\psi$	[0, 1]	0.2 ( $\leftrightarrow$ avoid) 0.8 ( $\downarrow$ avoid)	$K_\psi + K_z = 1$
Risk Tolerance in Obstacle Avoidance			
Param.	Range	Rec. Value	Restrictions
$r_{search}$	$> R_{drone}$	$1m \sim 1.5m$	$r_{search}(1 - \lambda_\psi) > R_{drone}$
$\lambda_\psi$	[0, 1]	0.5	$r_{search}(1 - \lambda_\theta) > H_{drone}$
$\lambda_\theta$	[0, 1]	0.75	
$\psi^{beam}$	[0, 180°]	90°	
$\theta_{max}^{beam}$	[0, 180°]	90°	

Dynamic Window Discretization		
Param.	Value	Restrictions
$v_x^{step}$	0.05m/s	Computation time and gross discretization
$v_z^{step}$	0.05m/s	
$\omega_z^{step}$	2.5°/s	

Hexarotor Physical Parameters		
Param.	Value	
$m$	3.65kg	
$R$	0.4m	
$H$	0.3m	

Hexarotor Dynamic Parameters		
Param.	Value	Restrictions
$v_x^{max}$	0.3m/s	
$v_z^{max}$	0.3m/s	
$\omega_z^{max}$	45°/s	
$\dot{v}_x^{max}$	1m/s <sup>2</sup>	
$\dot{v}_z^{max}$	1m/s <sup>2</sup>	
$\dot{\omega}_z^{max}$	100°/s <sup>2</sup>	Environment size and motors limits

Table 1: Main DWA parameters summary, with their admissible ranges and recommended values.

with three variants of the global planner is described: Naive (direct straight line to the goal), Not size-aware (the drone size is not considered), and Size-aware (the drone size is taken into account).

To enhance the flexibility of the system, the OMPL library [24] has been used as to implement the core of this subsystem, offering the chance to select between a wide number of SOTA global planning algorithms. The selected approach is RRT\* [21], based in Rapidly-Exploring Random Trees (RRT).

## 6. Experimental Results

In this section several experiments have been addressed for evaluating the performance of the proposed method in different situations. The main issue we want to evaluate is the capability of DWA-3D jointly with a global planner for avoiding the obstacles, following the global path planned if possible, complying the motion to the desired behavior of the avoidance, laterally or vertically, depending on the scenario, whilst ensuring always the drone safety, being the DWA-3D the one that makes the final motion decision.

### 6.1. Setup

The real experiments have been performed with a custom hexarotor (Figure 10) built with a DJI F550 frame. It has 0.8 m of diameter. As on-board computer

a Jetson Orin Nano Devkit has been mounted and a Pixhawk 4 has been in charge of the flight control. The sensing has been performed with an ouster OS0-32 3D LiDAR, which offers a vertical resolution of 32 planes of 1024 points each and a field of view of 360° × 90°. A GoPro is mounted aiming forward, enabling FPV (First Person View), for performing, for instance, inspection tasks. In order to decouple the localization and navigation problems, an Optitrack system has provided the position and orientation of the hexarotor in this work.

### 6.2. Parameters Configuration

As it has been shown along section 4, several parameters are involved in the DWA-3D computations. Table 1 shows a summary of the main parameters, suggested and used in the experiments. The maximum values of the velocities were restricted to those values according with the not very big size of the scenario and for ensuring safe maneuvers when the obstacles are very close. They could increased in the cases of larger environments and more clearance among the obstacles. On the other hand, the RRT\* safety distance (when used) has been established to  $\frac{r_{search}}{2}$ , being  $r_{search}$  the frontal safety distance used for the local planner, see Equation 17.

An initial orientative value for  $\alpha$ ,  $\beta$  and  $\gamma$  can be established by following a reasoned mathematical approach starting from Equation 10. Given that the UAV

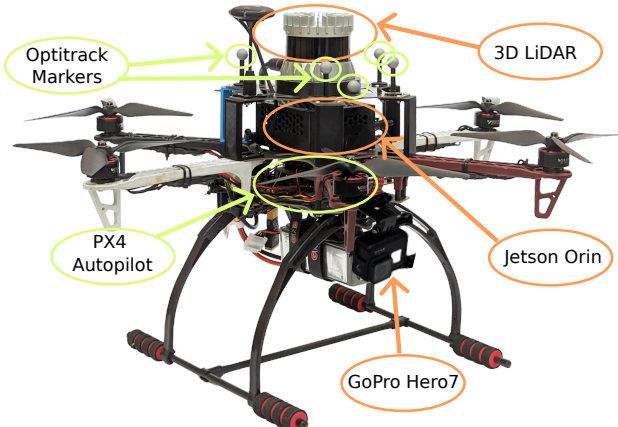


Figure 10: Custom hexarotor used to perform the real experiments, equipped with a OSO-32 3D LiDAR, a Jetson Orin Nano Devkit, a PX4 flight controller and GoPro Hero 7 for visual inspection.

is perfectly aligned both in height and orientation, it will score 1 in the normalized *Heading* term, so

$$G(\mathbf{v}) = \alpha + \beta \cdot Dist(\mathbf{v}) + \gamma \cdot Vel(\mathbf{v}) \quad (22)$$

If we dismiss the *Velocity* term, which could be feasible under certain circumstances,

$$G(\mathbf{v}) = \alpha + \beta \cdot Dist(\mathbf{v}) \quad (23)$$

In order to be able to avoid an obstacle that appears in front of the UAV; a velocity that pulls the drone away from the path and the obstacle must be selected, thus

$$\beta \cdot Dist(\mathbf{v}) > \alpha \quad (24)$$

So, if we want to be sure that the normalized *Distance* term scores 1 always it is possible, which ensures staying away from obstacles,

$$\beta > \alpha \quad (25)$$

Note that motion direction could need to change even 180° with respect to the goal to avoid certain dangers, this means even in the worst case for the *Head<sub>psi</sub>* term, the avoidance must be preferred if following the plan would lead to collision, thus considering that we are moving in a horizontal plane and combining Equation 17, Equation 18 and Equation 19:

$$\beta \frac{r_{search} \cdot \rho_{\psi}^{90^\circ} \cdot \rho_{\theta}^{0^\circ}}{r_{search}} + \alpha \cdot \frac{\omega_z^{max} \cdot \Delta t}{\pi} < \beta \quad (26a)$$

$$\beta \cdot (1 - \lambda_{\psi}) + \alpha \cdot \frac{\omega_z^{max} \cdot \Delta t}{\pi} < \beta \quad (26b)$$

$$\beta \cdot \lambda_{\psi} > \alpha \cdot \frac{\omega_z^{max} \cdot \Delta t}{\pi} \quad (26c)$$

that means that it must be preferred a velocity that avoids being penalized by the shortest horizontal ray (right side of Equation 26a) rather than one that aligns the drone by an angle of  $\omega_z^{max} \cdot \Delta t$  with the goal while touching the obstacle with that aforementioned ray (left side of Equation 26a). Note that  $R_{drone}$  has not been taken into account for the sake of simplicity, the committed error is accepted because we are computing a tentative value. Regarding  $\gamma$  value, it must be considered that higher speeds are desirable always that they do not involve a greater risk of collision nor worsen the preferred alignment:

$$\beta > \gamma \quad (27)$$

$$\alpha \cdot max(K_z, K_{\psi}) > \gamma \quad (28)$$

The values in Table 1 fit these constraints, which were considered in the adjustment process.

Regarding maximum accelerations, both rotors thrust capabilities ( $T_i$ ) and system mass ( $m$ ) must be considered. From [25],  $\dot{v}_x$  and  $\dot{v}_z$  can be expressed as:

$$\dot{v}_x = -\frac{K_{ftx}}{m} v_x + \frac{1}{m} u_x \sum_{i=1}^6 T_i \quad (29a)$$

$$u_x = \cos(\phi)\cos(\psi)\sin(\theta) + \sin(\phi)\sin(\psi), \quad (29b)$$

$$\dot{v}_z = -\frac{K_{ftz}}{m} v_z - g + \frac{\cos(\phi)\cos(\theta)}{m} \sum_{i=1}^6 T_i \quad (30)$$

where  $K_{ftx}$  and  $K_{ftz}$  are air resistance coefficients and  $g$  the gravity. To compute  $\dot{v}_x^{max}$  we can impose that  $\phi = 0$ ,  $\psi = 0$  and dismiss  $K_{ftx}$  and  $K_{ftz}$ ,

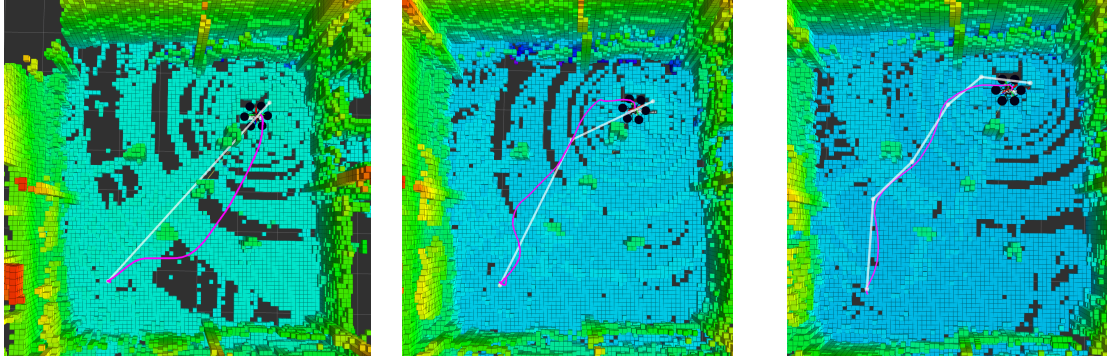
$$\dot{v}_x^{max} = \frac{\sum_{i=1}^6 T_i \sin(\theta)}{m} \quad (31)$$

$$\dot{v}_z^{max} = -g + \frac{\sum_{i=1}^6 T_i \cos(\theta)}{m} \quad (32)$$

If we suppose that  $\dot{v}_z = 0$  and limit the maximum pitch to  $\theta = 25^\circ$ , the throttle that each motor will be,

$$T_i(\theta = 25^\circ) = \frac{g \cdot m}{6 \cos(\theta)} = 6.57N \quad (33)$$

according to the motors' manufacturer this thrust is achieved with around 50% of throttle, which ensures a safe working point. Note that all motors are considered to be performing the same thrust because only forward



(a) Naive path (straight line); drone does not follow it, passing by the middle of two obstacles. (b) RRT\* NOT size aware path passing too near to obstacles; DWA-3D keeps the safety distance. (c) RRT\* size aware path avoiding the areas where the drone does not fit; it follows the planned path.

Figure 11: Global planning situations under which the DWA local planner has been tested. Planned path (white) and performed trajectory (purple) with the real-time updated Octomap after the flight. More intense green colour represents obstacles. Note that the map is not known beforehand, thus the path may pass near obstacles that initially were partially or fully occluded.

motion is considered here ( $\omega_z = 0$ ). Thus, the  $\dot{v}_x^{max}$  computation is straightforward,

$$\dot{v}_x^{max}(\theta = 25^\circ) = \frac{6 \cdot T_i \cdot \sin(\theta)}{m} = 4.5 \frac{m}{s^2} \quad (34)$$

so the restriction imposed because of the lab size fulfills this limit.

Under the previous scenario ( $\theta \leq 25^\circ$ ), supposing the UAV is accelerating with  $\dot{v}_x = \dot{v}_z = 1 \frac{m}{s^2}$ , and working with Equation 31 and Equation 32 the pitch angle will be,

$$\theta(\dot{v}_x = \dot{v}_z = 1 m/s^2) = \text{atan}\left(\frac{1}{1+g}\right) = 5.3^\circ \quad (35)$$

In this situation it is required a thrust of

$$T_i(\theta = 5.3^\circ) = \frac{m}{6\sin(\theta)} = 6.58N \quad (36)$$

Then, the imposed acceleration limits are achievable with the available hardware.

### 6.3. Experiments

The autonomous navigation of the drone has been tested in our "Unizar Drone Arena", a  $6 \times 6 \times 6$ m safe area. Several configurations with obstacles have been proposed under different circumstances and preferences. As one of our main contributions is the DWA-3D reactive navigator, three different navigation circumstances have been proposed in order to be able to analyze its performance and effect.

1. **Without global planner (Naive)**(Figure 11a): Under this configuration, the path that is given to the DWA-3D local planner is a straight line from the starting point of the drone to the desired final position, thus it must find the way to reach the goal only using reactive navigation.

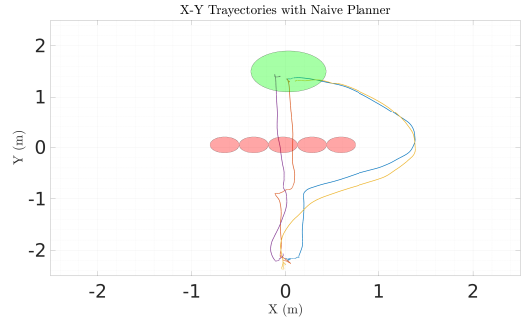
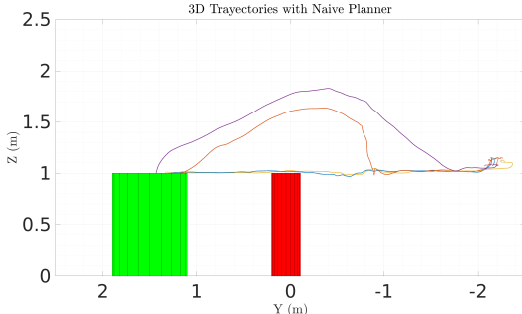
2. **With NOT size-aware global planner** (Figure 11b): A first approach to introduce a global planner has been without taking the drone size into account, which leads to paths that guide it towards the goal through short paths, but that could involve traversing dangerous areas that pass too near to obstacles.

3. **With size-aware global planner** (Figure 11c): Finally, a safer global planner has been integrated by leaving a safety distance between the planned path and the obstacles, thus gaps that are smaller than the drone size are avoided. Nevertheless, the DWA-3D reactive planner is still needed as the map is not known beforehand. The global path is computed using the initial UAV surroundings, so hidden obstacles would still represent a hazard if navigation only depended on the global planner.

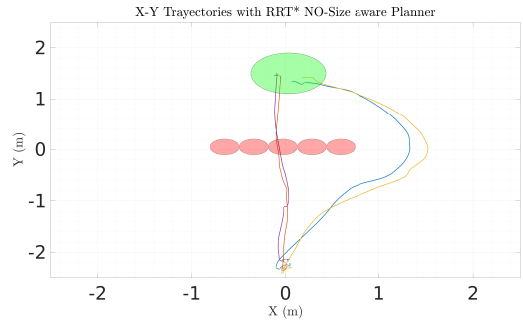
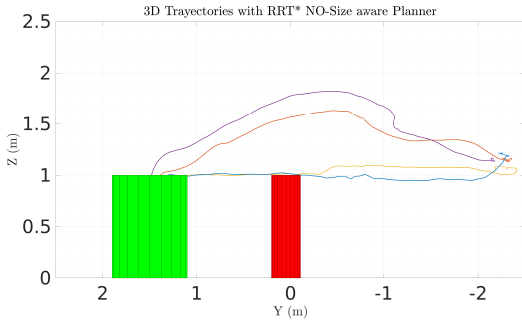
In every situation, DWA-3D makes the best final decision for maneuvering around the obstacles, following or not the global path, according with the safety criterium represented in the maximized objective function.

Those configurations have faced different scenarios with specific challenges to remark DWA-3D performance. Additionally, the capability of changing the avoidance preferences by tuning the parameters and its impact on the navigation have also been checked. As the area in which the flights are performed is limited, it has been decided to not allow the global planner to re-plan once it has provided the first solution, but it would be desirable to enable it when exploring longer environments like tunnels or caves, which will be applied in the future work.

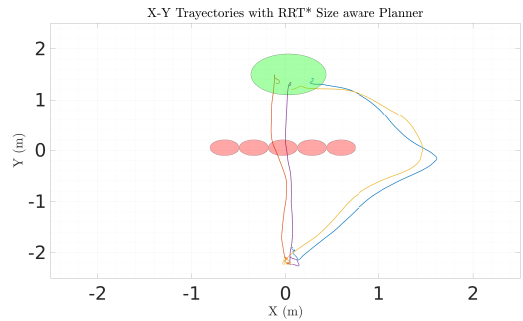
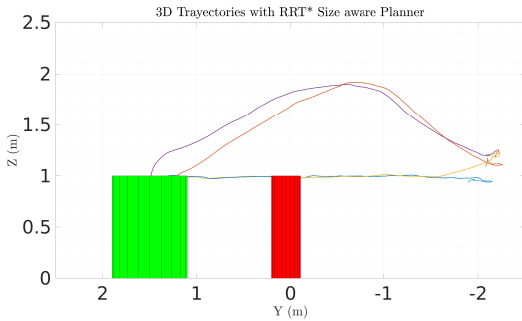
$-K_z > K_\psi$ , $r_{search} = 1\text{m}$	$-K_z > K_\psi$ , $r_{search} = 1.5\text{m}$	Obstacles
$-K_\psi > K_z$ , $r_{search} = 1\text{m}$	$-K_\psi > K_z$ , $r_{search} = 1.5\text{m}$	Goal



(a) Without global planner (Naive planner).



(b) RRT\* NOT size aware.



(c) RRT\* size aware.

Figure 12: Lateral and Top views for the trajectories performed in the *Wall Scenario* under  $r_{search}$ ,  $K_\psi$  and  $K_z$  combinations proposed in Table 1. Left,  $K_\psi = 0.8$ ,  $K_z = 0.2$  (purple and orange), keeping orientation is prioritized, therefore a vertical avoidance is executed; right,  $K_\psi = 0.2$ ,  $K_z = 0.8$  (blue and yellow), keeping orientation is relaxed, therefore a lateral avoidance is allowed. Red cylinders are obstacles and the green one is the goal.

### 6.3.1. Wall Scenario

The goal and the drone are separated by a wall of  $1m \times 1.5m \times 0.3m$  ( $H \times L \times W$ ) that can be avoided by flying over it or by passing by any of its sides. Although this scenario may not involve a challenge for an autonomous navigation system, it is the perfect situation to show the changes produced by variations in parameters. Figure 12a contains 4 trajectories (safer or riskier; lateral or vertical avoidance) following the naive plan while changing  $K_z$ ,  $K_\psi$  and  $r_{search}$  according to Table 1. It can be seen that for  $K_z > K_\psi$ , lateral avoidance is preferred because orientation to the goal is enforced to be kept; otherwise, vertical is. Moreover, it is manifested that the lower  $r_{search}$  is, the later is produced the reaction to the obstacle, as it is considered at a lower distance.

Then, the same flights are performed with a global planner that does not consider the drone's size, Figure 12b. It can be seen that after adding the global planner, the obstacle evasion starts earlier than before, no matter the value of  $r_{search}$ . Nevertheless, as those plans tend to lead to lateral collision (UAV's dimensions were not considered), DWA-3D must react and avoid them. That phenomena is reflected as a *two-steps* avoidance, the first and inaccurate one performed by the global planner and the one that ensures the safe operation due to DWA-3D intervention. Is in this second step where the effect of the  $r_{search}$  value influences.

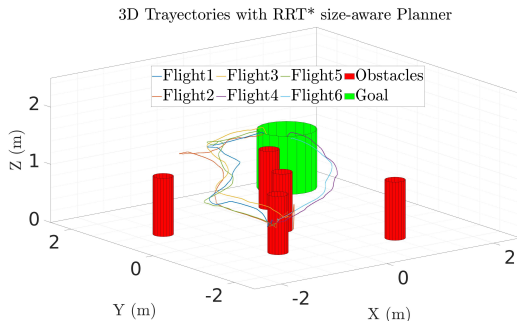
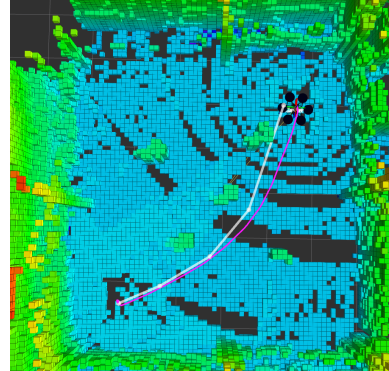


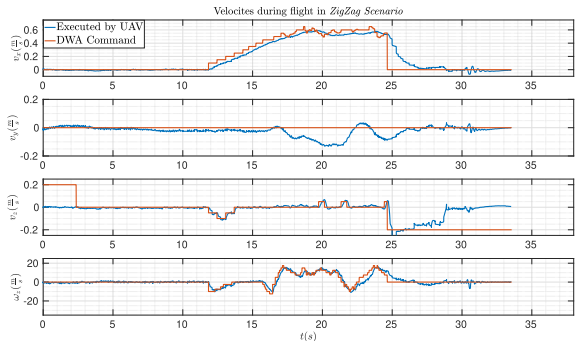
Figure 13: 3D trajectories in *Zigzag Scenario* with the RRT\* size aware. Red cylinders are obstacles and the goal is the green one.

Finally, the global planner is configured such in a way that it considers the drone's size, computing safer paths, Figure 12c. Although now the difference of selecting a value more conservative or more riskier for  $r_{search}$  is subtle, we can still observe two phases during obstacle avoidance and that the second one is influenced by it. While the global path is within the known region, the UAV just have to follow it, as it is safe. Once it arrives to a region that was unknown when the path was computed, the effect  $r_{search}$  value is translated as a faster and

less conservative or slower and more careful approach to the goal.



(a) Performed trajectory (purple) and global plan (white). Note in the top figure the upper obstacle is not seen from the initial point of view, when the global plan was computed at the beginning and it does not change (replan disabled) but the DWA-3D avoids it. [VIDEO](#).

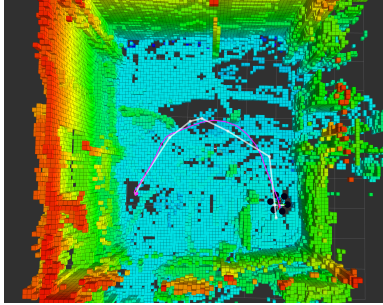


(b) Velocities profiles during a flight in the *ZigZag Scenario* with  $v_x^{max} = 0.75 \frac{m}{s}$ . In red, the one commanded by the local planner (DWA-3D); in blue the ones executed by the UAV.

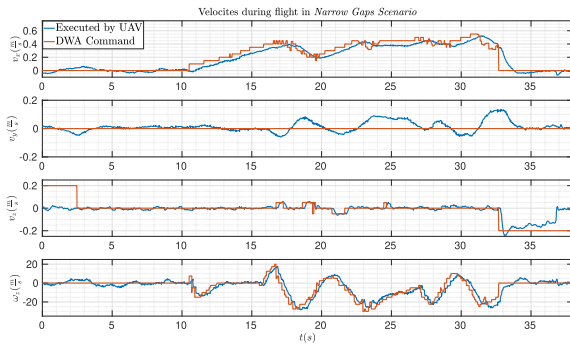
Figure 14: Flight in the *ZigZag Scenario* (top) and velocities (desired and executed) during it (bottom).  $v_x^{max}$  has been increased from  $0.3 \frac{m}{s}$  to  $0.75 \frac{m}{s}$  with respect to experiments in Figure 13.

### 6.3.2. ZigZag Scenario

A set of five cylinders are placed as obstacles between the drone's initial position and its destination, forcing it to maneuver through them in a zig-zag pattern. This configuration has been designed in such a way that it allows performing different but similar trajectories, exhibiting the randomness inherent the RRT-based global planners, Figure 13. Additionally, in Figure 11, the results using the three global planner options can be observed. Once, it has been checked that the system is able to navigate safely under this circumstances,  $v_x^{max}$  has been increased from  $0.3 \frac{m}{s}$  to  $0.75 \frac{m}{s}$ , allowing to perform more agile flights, Figure 14.



(a) Performed trajectory (purple) and global plan (white). Note in the top figure the Octomap had unknown areas when the global plan was computed at the beginning and it does not change (replan disabled).



(b) Velocities profiles during a flight in the *Narrow Gaps Scenario* with  $v_x^{max} = 0.75 \frac{m}{s}$ . In red, the one commanded by the local planner (DWA-3D); in blue the ones executed by the UAV.

Figure 15: Flight in the *Narrow Gaps Scenario* (top) and velocities (desired and executed) during it (bottom). [VIDEO](#)

### 6.3.3. Narrow Gaps Scenario

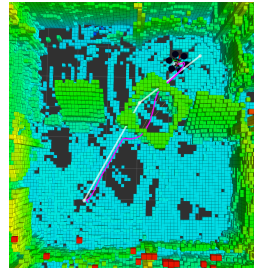
In this scenario, the hexarotor must fly while overcoming sparse but nearby obstacles, by traversing through narrow gaps ( $1.25m \sim 1.35m$ ), having about 25 cm of clearance on each side in the worst case. Additionally, the maximum allowed  $v_x$  have been increased to  $0.75 \frac{m}{s}$ . Again, as flying over the obstacles would enable solving the maze without difficulties moving directly towards the goal, only lateral avoidance is favoured in this scenario. The performed trajectory along with the global plan and the velocities profiles (commanded by DWA and executed by the UAV) are shown in Figure 15.

### 6.3.4. Rings

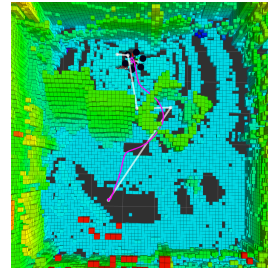
In order to exploit the drone capabilities, a more complicated navigation scenario through rings is proposed, see Figure 16a. Two variations were tested: a straight pass-through (Figure 16b) and a side exit through a lateral ring (Figure 16c). Here RRT\* safety distance has been reduced to  $0.2m$  instead of  $0.5m$  to enhance paths passing inside the ring as tolerance here is tighter. The



(a) Drone seen from behind traversing the rings.



(b) Pass-through flight.  
[VIDEO](#).



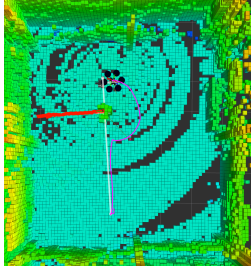
(c) 90° between rings flight.  
[VIDEO](#).

Figure 16: Top: UAV in the *Rings Scenario*. Bottom: Trajectories executed (purple) and global planner path (white) in rings scenario, lateral avoidance selected and  $r_{search} = 1m$ .

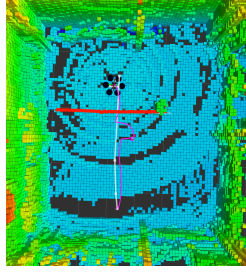
drone follows the planned paths between subgoals when possible, keeping the safety distance.

### 6.3.5. Moving obstacle

Finally, although DWA-3D is not tailored for highly dynamic scenarios, we want to explore the capability of dodging moving obstacles. It has been studied by interrupting the trajectory of the UAV with a TurtleBot 2 platform with a cylinder tied to its top plate. Initially, the UGV remains static and allows the drone's global planner to compute a path. Once the hexarotor has a plan and starts following it, the roomba moves at a constant speed ( $0.3 \frac{m}{s}$ ), enforcing the DWA-3D to react and avoid it, see Figure 17. Two cases are represented, in the first one the UGV stops once it cuts the UAV trajectory; while in the second one it (UGV) keeps moving forward. A lateral avoidance is selected and  $r_{search} = 1.5m$ . During the experiments in this scenario it has been noticed that Octomap does not update the dynamic changes in the scene at the moment. As the occupancy map is updated regarding the occupancy proba-



(a) The UGV stops once it has interrupted the UAV path. The drone avoids the new obstacle. [VIDEO](#).



(b) UGV keeps moving and blocks the UAV movement for a longer time until the room is opened again, then the drone keeps its path. [VIDEO](#).

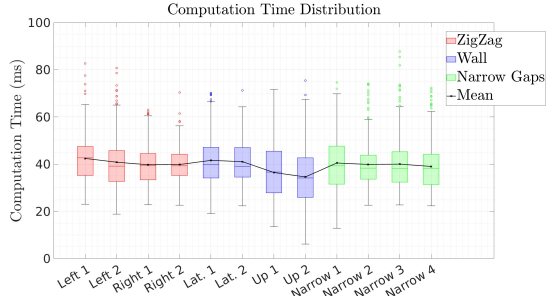
Figure 17: Trajectories executed by the UAV(purple) and global planner path (white) computed when the UGV is in the left part of the red trajectory shown, and so the room to the goal is free.

bilities given the sensor measurements and the previous information, those changes in the scene take some time to be considered as real and not only as sensor noise. This involves a noticeable delay while refreshing the position of the UGV, thus taking more time and maneuvers to avoid.

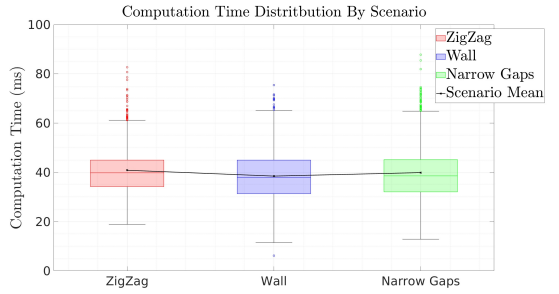
#### 6.4. Discussion

Apart from the maximum velocities and acceleration dependent on the specific drone, a few set of parameters have to be tuned to change the desired behaviour related with obstacle avoidance. Lower  $r_{search}$  values allow passing through narrower gaps in exchange of assuming higher risks while avoiding obstacles, as a minor safety distances are kept (frontal, vertical and lateral). The difference is even more noticeable when obstacles that were not observed during global planning are dodged. RRT\* global planner may retrieve sub-optimal plans when the path traverses partially or fully unknown areas. This could be tackled by allowing re-planning periodically, which was not allowed due to the reduced size of the arena where the experiments were performed. Global and local planner integration along with providing UAV size awareness to the global planner allows performing smoother and more direct trajectories; combining their virtues and compensating their weaknesses.

A wide number of experiments have been performed, using the three planners, and different values of the weighting parameters in the objective function in DWA-3D local planner. From those experiments, we concluded that the values shown in Table 1, are the ones that best adapt to all the encountered situations, moreover having an intuitive meaning. Therefore it is very



(a) Computation time distribution for each individual flight.



(b) Computation time distribution grouped by scenario.

Figure 18: DWA computation time distribution in 3 scenarios (ZigZag, Wall and Narrow Gaps) for 4 consecutive flights in each one.

easy to tune or change to modify the desired avoidance behavior.

Regarding DWA-3D computation time, it has been measured in *ZigZag*, *Wall* and *Narrow Gaps* scenarios during the execution of four consecutive flights each, see Figure 18. It does not only remain bounded under 100ms, but also it has small variability, being stable about 40ms (both mean and median) in every flight and scenario.

The code used for this research will be made available upon publication acceptance <https://github.com/JBesCar/Dwa3D>. This will enable researchers to reproduce the results and facilitate further development in this field.

## 7. Conclusions and future work

In this work a new DWA-3D local planning algorithm has been developed for UAV navigation to obtain great maneuverability in narrow rooms among obstacles. It has been integrated along with a RRT\* global planner. The drone is located by means an Optitrack system for an accurate localization, to decouple the localization and navigation problems, being the latter the focus of this work. Avoidance preference can be adjusted to lateral or vertical evasion of the obstacles by balancing

the values of two parameters  $K_\psi$  and  $K_z$  in the objective function optimization. The constraints for the parameters have been analytically analyzed, and a set of parameter values for proper configuration have been provided along with a well-tested and configurable code in ROS. Real experimentation has been performed using a custom-built hexarotor equipped with a 3D-LiDAR. Different scenarios have been built, successfully navigating between narrow gaps and in a lightly changing scenario.

The navigation performance in the case of moving obstacles are present is limited by the Octomap refresh rate. Thus, a faster local map representation would be desirable to navigate in more complex and dynamic dynamic scenarios. Moreover, we plan to integrate a localization method into the system in order to replace the Optitrack system and perform missions in larger environments, in particular in GPS-denied scenarios such as caves or tunnels.

## Acknowledgments

This work was partially supported by the Spanish projects PID2022-139615OB-I00/MCIN/AEI/10.13039/501100011033/FEDER-UE, and DGA-T45-23R.

## Declaration of generative AI and AI-assisted technologies in the writing process.

During the preparation of this work the authors used Gemini in order to improve text readability. After using this tool, the authors reviewed and edited the content as needed and take full responsibility for the content of the published article.

## References

- [1] L. Kapustina, N. Izakova, E. Makovkina, M. Khmelkov, The global drone market: main development trends, in: SHS Web of Conferences, Vol. 129, EDP Sciences, 2021, p. 11004.
- [2] J. Shahmoradi, E. Talebi, P. Roghanchi, M. Hassanalian, A comprehensive review of applications of drone technology in the mining industry, *Drones* 4 (3) (2020) 34.
- [3] J. Xing, G. Cioffi, J. Hidalgo-Carrió, D. Scaramuzza, Autonomous power line inspection with drones via perception-aware mpc, in: 2023 IEEE/RSJ International Conference on Intelligent Robots and Systems (IROS), 2023, pp. 1086–1093.
- [4] M. Roca-Riu, M. Menendez, Logistic deliveries with drones: State of the art of practice and research, in: 19th Swiss Transport Research Conference (STRC 2019), STRC, 2019.
- [5] X. Liu, S. W. Chen, G. V. Nardari, C. Qu, F. Cladera, C. J. Taylor, V. Kumar, Challenges and opportunities for autonomous micro-uavs in precision agriculture, *IEEE Micro* 42 (1) (2022) 61–68.
- [6] H. Surmann, I. Kruijff-Korbayova, K. Daun, M. Schnaubelt, O. von Stryk, M. Patchou, S. Boecker, C. Wietfeld, J. Quenzel, D. Schleich, S. Behnke, R. Grafe, N. Heidemann, D. Slomma, Lessons from robot-assisted disaster response deployments by the german rescue robotics center task force (2022). *arXiv: 2212.09354*.
- [7] F. J. Perez-Grau, R. Ragel, F. Caballero, A. Viguria, A. Ollero, An architecture for robust uav navigation in gps-denied areas, *Journal of Field Robotics* 35 (1) (2018) 121–145.
- [8] B. Lindqvist, S. S. Mansouri, J. Haluška, G. Nikolakopoulos, Reactive navigation of an unmanned aerial vehicle with perception-based obstacle avoidance constraints, *IEEE Transactions on Control Systems Technology* 30 (5) (2021) 1847–1862.
- [9] B. Lindqvist, J. Haluska, C. Kanellakis, G. Nikolakopoulos, An adaptive 3d artificial potential field for fail-safe uav navigation, in: 2022 30th Mediterranean conference on control and automation (MED), IEEE, 2022, pp. 362–367.
- [10] J. Tordesillas, J. P. How, PANTHER: Perception-aware trajectory planner in dynamic environments (2021). *arXiv: 2103.06372*.
- [11] J. Tordesillas, J. P. How, FASTER: Fast and safe trajectory planner for navigation in unknown environments, *IEEE Transactions on Robotics* (2021).
- [12] M. Pantic, I. Meijer, R. Bähnemann, N. Alatur, O. Andersson, C. Cadena, R. Siegwart, L. Ott, Obstacle avoidance using ray-casting and riemannian motion policies at khz rates for mavs, in: 2023 IEEE International Conference on Robotics and Automation (ICRA), 2023, pp. 1666–1672.
- [13] L. Lu, C. Sampedro, J. Rodriguez-Vazquez, P. Campoy, Laser-based collision avoidance and reactive navigation using rrt\* and signed distance field for multirotor uavs, in: 2019 international conference on unmanned aircraft systems (ICUAS), IEEE, 2019, pp. 1209–1217.
- [14] T. Elmokadem, A. V. Savkin, A hybrid approach for autonomous collision-free uav navigation in 3d partially unknown dynamic environments, *Drones* 5 (3) (2021) 57.
- [15] M. T. Ohradzansky, J. S. Humbert, Lidar-based navigation of subterranean environments using bio-inspired wide-field integration of nearness, *Sensors* 22 (3) (2022) 849.
- [16] D. Dirckx, M. Bos, W. Decré, J. Swevers, Optimal and reactive control for agile drone flight in cluttered environments, *IFAC-PapersOnLine* 56 (2) (2023) 6273–6278.
- [17] D. Fox, W. Burgard, S. Thrun, The dynamic window approach to collision avoidance, *IEEE Robotics & Automation Magazine* 4 (1) (1997) 23–33.
- [18] I. Tusseyeva, S.-G. Kim, Y.-G. Kim, 3d global dynamic window approach for navigation of autonomous underwater vehicles, *International Journal of Fuzzy Logic and Intelligent Systems* 13 (2) (2013) 91–99.
- [19] C. Lin, Y. Liu, S. Lin, An adaptive dynamic window approach for uuv obstacle avoidance planning in 3d environments, *Journal of Physics: Conference Series* 2704 (1) (2024) 012026.
- [20] X. Wang, M. Cheng, S. Zhang, H. Gong, Multi-uav cooperative obstacle avoidance of 3d vector field histogram plus and dynamic window approach, *Drones* 7 (8) (2023) 504.
- [21] S. Karaman, E. Frazzoli, Sampling-based algorithms for optimal motion planning (2011). *arXiv: 1105.1186*.
- [22] A. Hornung, K. M. Wurm, M. Bennewitz, C. Stachniss, W. Burgard, OctoMap: An efficient probabilistic 3D mapping framework based on octrees, *Autonomous Robots* (2013).
- [23] M. Quigley, K. Conley, B. P. Gerkey, J. Faust, T. Foote, J. Leibs, R. Wheeler, A. Y. Ng, ROS: An open-source robot operating system, in: Workshops at the IEEE International Conference on Robotics and Automation, 2009.

- [24] I. A. Şucan, M. Moll, L. E. Kavraki, The Open Motion Planning Library, *IEEE Robotics & Automation Magazine* 19 (4) (2012) 72–82.
- [25] M. Moussid, A. Sayouti, H. Medromi, Dynamic modeling and control of a hexarotor using linear and nonlinear methods, *International Journal of applied information systems* 9 (5) (2015) 9–17.